pH-Control Azadirachta indica Leaf Extract-Mediated Synthesis of Iron oxide Nanoparticles for Catalytic Degradation of Toxic Dyes and Biomedical Potential

Malti Gurjar
Uka Tarsadia University
Hitesh Rajput
Uka Tarsadia University
Abhitosh Kedia
Abhitosh.kedia@utu.ac.in
Uka Tarsadia University
Dimple Shah
SVNIT
Ishpal Rawal
Kirori Mal College, University of Delhi

Research Article

Keywords: Brunauer-Emmett-Teller (BET), Antioxidant, Catalytic activity

Posted Date: April 15th, 2026

DOI: https://doi.org/10.21203/rs.3.rs-9074312/v1

Additional Declarations: No competing interests reported.

pH-Control *Azadirachta indica* Leaf extract mediated synthesis of Iron oxide nanoparticles for catalytic degradation of toxic dyes and biomedical potential

Malti Gurjar[1], Hitesh Rajput[1, b], Abhitosh Kedia[1, a], Dimple Shah[2], Ishpal Rawal[3]

[1]*Department of Physics, Uka Tarsadia University, Bardoli, Surat-394350, Gujarat, India*

[2]*Department of Physics, SVNIT, Surat-395007, Gujarat, India.*

[3]*Department of Physics, Kirori Mal College, University of Delhi, Delhi-110007, India.*

[a]Abhitosh.kedia@utu.ac.in; Tel:+91 8780357578

[b]hitesh.rajput@utu.ac.in; Tel: +91 9727561617

Malti Gurjar (ORCID ID: 0009-0001-3230-6595)

Hitesh Rajput (ORCID ID: 0000-0002-2216-5506)

Abstract: Green synthesis offers an eco-friendly and sustainable route to nanoparticle fabrication by harnessing plant-derived phytochemicals as natural reducing and capping agents. In the present study, iron oxide nanoparticles (IONPs) were biosynthesized using *Azadirachta indica* (neem) leaf extract under varying pH conditions (3, 6, and 11), demonstrating the profound influence of reaction environment on nanoparticle formation and stability. Multifaceted characterization using UV–Vis spectroscopy, DLS, zeta potential, FESEM, FTIR, XRD, and BET confirmed the formation of stable, highly crystalline iron oxide nanoparticles. pH 6 yielded uniformly dispersed nanorods (50-80 nm broad, 10-20 μm long) with the maximum stability (-28.3 mV). Antioxidant assays showed significant radical scavenging activity, with IC_{50} values of 78.06 μg/mL (DPPH) and 70.94 μg/mL (ABTS). Catalytic studies revealed effective degradation of methylene blue and eosin yellow dyes, achieving removal efficiencies of ~62% and ~55% without H_2O_2, and ~87% and ~83% with H_2O_2 at room temperature within 60 min. These findings highlight the potential of *A. indica*-mediated IONPs as eco-friendly catalysts for wastewater treatment and as promising agents for biomedical applications.

Keywords: Brunauer-Emmett-Teller (BET), Antioxidant, Catalytic activity.

Introduction:

Recent developments in nanoscience and nanotechnology have yielded effective nanomaterials that exhibit remarkable properties in various applications, including drug delivery, soil remediation, water treatment, and catalysis [1]. The enhanced activity observed with decreasing nanoparticle size is attributed to the increased surface-to-volume ratio and pronounced alterations in physicochemical properties at the nanoscale. Iron-based nanoparticles have attracted considerable attention in contemporary research owing to their exceptional chemical and thermal stability, minimal toxicity, and unique magnetic behaviour [2-3].

Owing to their importance, various approaches, including chemical, physical, and photochemical methods, have been explored for the efficient and rapid synthesis of nanoparticles. However, these traditional methods are often costly and depend on toxic chemicals, harmful organic solvents, and non-biodegradable stabilizers [4-5]. Therefore, developing and adopting alternative green synthesis methods with minimal or no adverse effects on the environment and human health is crucial [6-7]. Consequently, researchers increasingly focus on plant-based green synthesis techniques for large-scale nanoparticle production, due to the abundance and accessibility of plant materials and their derivatives. This approach is characterized by its simplicity, environmental friendliness, stability, speed, and cost-effectiveness, utilizing water as a universal solvent to produce biocompatible nanoparticles. Notably, plant-mediated synthesis is usually performed at room temperature, unlike microbe-mediated synthesis, which requires heating of the reaction mixture or culture medium. Nanoparticles can be synthesized using diverse plant-derived materials, including leaves, stems, roots, flowers, and fruits, as well as their corresponding extracts [8-12]. Plant extracts facilitate the quick and easy production of nanoparticles with precise control over size, shape, morphology, and high yield in a single step [13-15].

Biomolecules or phytochemicals found in plants, such as proteins, amino acids, vitamins, flavonoids, polyphenols, tannins, terpenoids, alkaloids, polysaccharides, and saponins, are responsible for reducing metal salts [16]. Moreover, these bioactive compounds act as capping and stabilizing agents, providing nanoparticles with improved resistance to oxidation and agglomeration [17–19]. Several studies have shown that the phytochemicals in plants can function as both reducing and capping agents, allowing the formation of stable nanoparticles without requiring additional polymers or surfactants [20].

The biosynthesis of iron-based nanoparticles via plant extracts proceeds through a facile mechanism, wherein bioactive phytochemicals in the extract mediate the reduction of metal precursors and stabilize the resulting nanoparticles under precisely controlled reaction parameters (Figure 3). The reaction is finished within minutes or hours and the formation of nanoparticles can be concluded with the colour change of the reaction solution. Various synthesis parameters such as type and concentration of phytochemicals, metal salt concentration, pH, temperature etc [21-24]. Control nanoparticle formation along with their yield and stability. These parameters can be manipulated to synthesize nanoparticles with specific application-based properties [25-26].

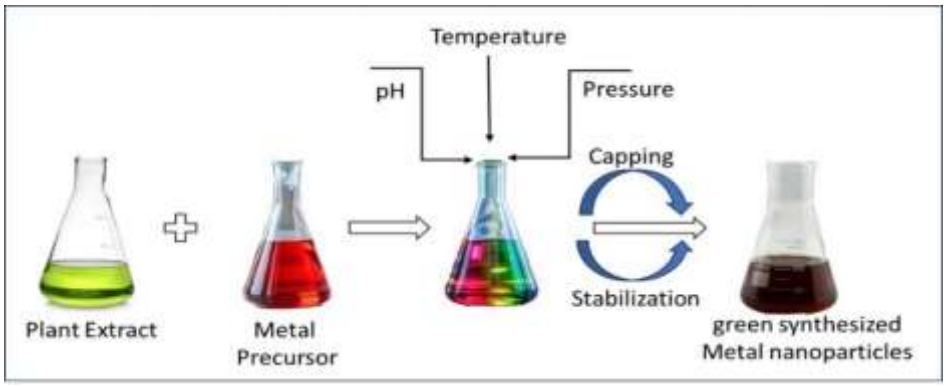

Figure 1: *Mechanism of Green Synthesis by Plant Extracts.*

Plants can accumulate specific concentrations of heavy metals in their tissues, enabling their use in biosynthetic processes. Consequently, plant-based methods for nanoparticle synthesis

have gained recognition as simple, efficient, cost-effective, and practical alternatives to conventional approaches. These methods leverage plant extracts to reduce and stabilize metallic nanoparticles in a single-step ("one-pot") synthesis process, utilizing a wide range of plant species.

Similarly, the green synthesis of iron and iron oxide nanoparticles has made use of various leaf, root, and fruit waste extracts (summarised in Table 1). The creation of metal nanoparticles is significantly influenced by the quantities and combinations of biomolecules utilised in these extracts.

Table 1: Reported green synthesis of iron nanoparticles using various plant extracts.

Plants	Size(nm)	Types	Application	References
Green Tea	40-60	Leaves	Catalytic Adsorption and Antibacterial	[27]
plantain peel extract	50	peel	Magnetic Properties	[28]
Mimosa pudica	~65	root	Magnetic Properties	[29]
Punica granatum and *Artocarpus heterophyllus*	20-30	Peel	Catalytic Adsorption and Antioxidant Activity	[30]
Platanus orientalis	78–80	Leaves	antifungal activity	[31]
watermelon	20	rinds	Catalytic Adsorption	[32]
Madhuca indica	55-60	plant	Cytotoxic, Antioxidant, Anti-Inflammatory, and Anti-Diabetic Properties	[33]

Common organic pollutants such as 2,4,6-trinitrotoluene (TNT), carbon tetrachloride, trichloroethene, and many more may be effectively removed by iron oxide nanoparticles (IONPs), and their use in environmental remediation has become more well-known [34-36]. Pb (II) and Cr (VI) are two heavy metals that may be successfully eliminated from groundwater [36-39]. To eliminate these contaminants and purify water, a wide range of physical and chemical techniques have been used in the past, including membrane filtration, electrochemical treatment, adsorption, chemical precipitation, and oxidation processes [40]. However, most of these methods are either very costly or ineffective [40-42]. Iron oxide nanoparticles (IONPs) act predominantly as Fenton-like catalysts, facilitating the oxidative breakdown of various organic pollutants and dyes. Recent research emphasizes the importance of Fenton-like processes for the effective removal of organic contaminants under mild reaction conditions [43]. In contrast to the traditional Fenton reaction, which depends on soluble ferrous ions, this eco-friendly approach generates hydroxyl radicals *in situ* through the interaction of hydrogen peroxide with iron oxide or zero-valent iron nanoparticles, providing a more sustainable and efficient route for environmental pollutant degradation [44–45].

The present study investigates the eco-friendly synthesis of IONPs utilizing the aqueous extract of *Azadirachta indica (AI)*. This plant is abundant in various phytoconstituents, including alkaloids, flavonoids, phenols, gallic acid, polyphenols, and nimbins [46]. *AI* is notably rich in polyphenolic compounds, which function as both reducing and stabilizing agents in

nanoparticle synthesis. The resulting IONPs were comprehensively characterized using advanced techniques, including UV–visible spectroscopy (UV–Vis), dynamic light scattering (DLS) with zeta potential analysis, field emission scanning electron microscopy (FESEM), Fourier-transform infrared spectroscopy (FTIR), and Brunauer–Emmett–Teller (BET) surface area analysis. These studies confirmed that the green-synthesised IONPs exhibit significant antioxidant activity, as evidenced by 2,2-diphenyl-1-picrylhydrazyl (DPPH) and 2,2′-azino-bis(3-ethylbenzothiazoline-6-sulfonic acid) (ABTS) assays, highlighting their potential as effective antioxidant agents. Furthermore, the catalytic activity of the IONPs was evaluated as Fenton-like catalysts for the degradation of anionic (Eosin Yellow, EY) and cationic (Methylene Blue, MB) dyes, demonstrating their applicability in environmental remediation.

Materials and Methods:

Materials:

Fresh *Azadirachta Indica (AI)* leaves were collected from the Uka Tarsadia University campus in Bardoli, Gujarat, India. The chemicals used in this study, along with their molecular weights, included Ferric chloride ($FeCl_3$, 162.2 g/mol), MB (319.85 g/mol), EY (647.89 g/mol), sodium hydroxide (NaOH, 40 g/mol), and hydrochloric acid (HCl, 36.50 g/mol) from Loba Chemical Pvt. Ltd. For antioxidant assays, DPPH (394.32 g/mol) and ABTS (548.68 g/mol), along with potassium persulfate ($K_2S_2O_8$, 270.32 g/mol), were obtained from Sisco Research Laboratory Pvt. Ltd. Millipore water was used throughout all synthesis and experimental procedures.

Methods:

Leaves Extract Preparation:

Azardirachta indica (AI) was harvested individually, cleaned many times with water to get rid of any dirt, and then let dry in the sun to get rid of any moisture before being ground into a powder. 100 millilitres of Millipore water and five grams of fine powder of dried *AI* were subjected to sonication for 20 minutes. The extract was then passed through Whatman No. 1 filter paper, preserved at 4 °C, and later employed for the synthesis of nanoparticles (Figure 2).

Green Synthesis of IONPs from Leaves Extract:

To synthesize IONPs, a 0.1 M $FeCl_3$ solution prepared in distilled water was gradually mixed with the AI leaf extract in a 1:2 volume ratio at room temperature under constant stirring. The colour changes of the mixture from yellow to black within one hour signified the successful formation of IONPs, which was subsequently verified using UV–Vis spectroscopy of the produced iron oxide colloidal solution (Figure 2).

Figure 2: *Schematic diagram of the step-by-step formation of IONP nanoparticles*

Methodology of Catalytic Activity:

The catalytic effectiveness of the produced IONPs has been examined for the elimination of the cationic dye MB and the anionic dye EY, which is commonly utilized in the textile sector. A total of 10 mg of the synthesized iron oxide nanoparticles were introduced to 40 mL of MB and EY solutions at concentrations of 30 µM and 25 µM, respectively. The mixture was incubated for numerous amounts of time (0-70 min) at 298 K (Figure S1). With the measurement of MB and EY concentration at different time intervals, the adsorption ability of iron oxide nanoparticles was investigated using the formula [47].

$$\text{catalytic activity (\%)} = \left(\frac{A_0 - A}{A}\right) \text{x}100$$

where A_0 (pure Dye) and A remaining Dye (after the addition of iron oxide nanoparticles in the presence of H_2O_2 and absence of H_2O_2 respectively) were the absorbances at 664 nm for MB and 520 nm for EY as measured by UV-Vis. spectra.

Antioxidant Studies:

Determination of 2,2-diphenyl-1-picrylhydrazyl (DPPH) free radical scavenging assay:

The antioxidant potential of the green-synthesized IONPs was evaluated at varying concentrations using the DPPH assay [48–49]. Briefly, different doses of IONPs (25–150 µg/mL) were added to 2 mL of 0.25 mM methanolic DPPH solution and incubated in the dark at room temperature for 30 min (Figure S2). The reduction of DPPH was monitored spectrophotometrically by the colorimetric change from purple to yellow, corresponding to a decrease in absorbance at 517 nm, the characteristic peak of DPPH. This decolourization indicates effective electron transfer from the IONPs to the DPPH radicals, confirming their significant free radical scavenging activity [50].

Determination of ABTS radical cation scavenging activity:

Green-synthesized iron oxide nanoparticles (IONPs) were assessed for their radical cation scavenging ability using the ABTS assay [49, 51]. The ABTS radical cation ($ABTS^{\bullet+}$) was produced by combining 10 mM ABTS with 3.5 mM potassium persulfate (APS) and allowing the mixture to react in the dark at ambient temperature for 16 hours. The obtained solution was

then diluted with methanol to attain an absorbance of 1.40 ± 0.05 at 745 nm. Subsequently, varying concentrations of the synthesized IONPs (25–150 µg/mL) were introduced into 2 mL of the prepared ABTS solution and incubated in the dark at room temperature for 10 minutes (Figure S3). The antioxidant activity was evaluated spectrophotometrically by measuring the reduction in absorbance at 745 nm. The observed colour changes from blue-green to light green or colourless indicated effective $ABTS^{\bullet+}$ radical quenching. The antioxidant performance of the IONPs was further compared with the standard antioxidant butylated hydroxyanisole (BHA), demonstrating their significant radical scavenging potential.

The percentage inhibition for the DPPH and ABTS radical scavenging activity was calculated using the following formula,

$$\textbf{\textit{Percentage inhibition}} = \frac{(\textbf{\textit{Control Abs.}} - \textbf{\textit{Sample Abs.}})}{\textbf{\textit{Control Abs.}}} \textbf{ x } \textbf{\textit{100}}$$

Result and Discussion:

The reduction of the metal precursor into IONPs using *AI* leaf extracts was observed as its colour shifts from pale yellow to either dark brown or black. The reaction was completed within two hours after the metal ions were added to the *AI leaf* extract. Further solution pH significantly influences the optical and morphological properties of the nanoparticles because of the kinetics of nanoparticle formation [52].

Uv-Vis. Spectroscopy:

The UV-Vis spectra for IONPs synthesized at pH 3, pH 6, and pH 11 exhibit absorption peaks in the UV region around 270–275 nm. This indicates the successful formation of iron oxide nanoparticles, as metal oxides generally absorb strongly in this region due to electronic transitions. Higher absorbance intensity at pH 6 suggests greater nanoparticle concentration and more uniform distribution of particles, (likely due to optimal synthesis conditions at neutral pH) the broader peaks at pH 3 and pH 11 indicate less uniformity and potential aggregation of particles due to uneven adsorption of organic groups on particle surfaces, which leads to irregular shapes and non-uniform distributions.

The band gap of IONPs was also measured through the Tauc plot of the UV-Vis spectra, which were found to be 3.24ev, 2.53ev, and 3.00ev for 3pH, 6pH, and 11pH, respectively [55]. The lower band gap at pH 6 reflects larger and more uniformly distributed particles, attributed to controlled growth conditions at neutral pH.

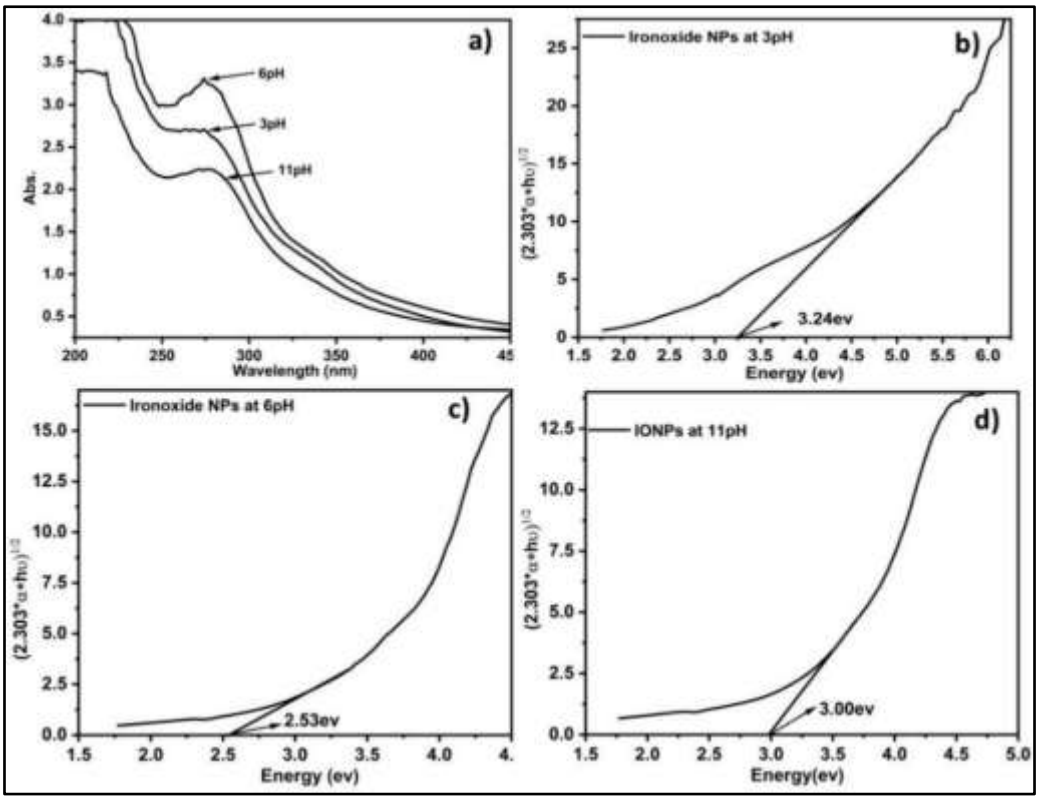

Figure 3: *(a) UV–Vis spectra of iron oxide nanoparticles synthesized using Azadirachta indica leaf extract at various pH levels; (b) Tauc plot for optical band gap estimation at pH 3; (c) at pH 6; and (d) at pH 11.*

Field Emission Scanning Electron Microscopy (FE-SEM):

FE-SEM images provide detailed insights into the morphology and size of the synthesized IONPs (Figure 4). At pH 3 and 11, the nanoparticles appear irregularly shaped, a result of uneven growth in the acidic and basic medium. At pH 6, uniform nanorods are observed, with dimensions of 50–80 nm in width and 10–20 μm in length, indicating optimal synthesis conditions where even nucleation and growth, result in consistent morphology. These morphological differences align with the optical properties and highlight the importance of pH in controlling nanoparticle shape and size. The differences in particle size and non-uniformity seen in the FESEM images can be linked to the uneven adsorption of organic groups on the surface of IONPs.

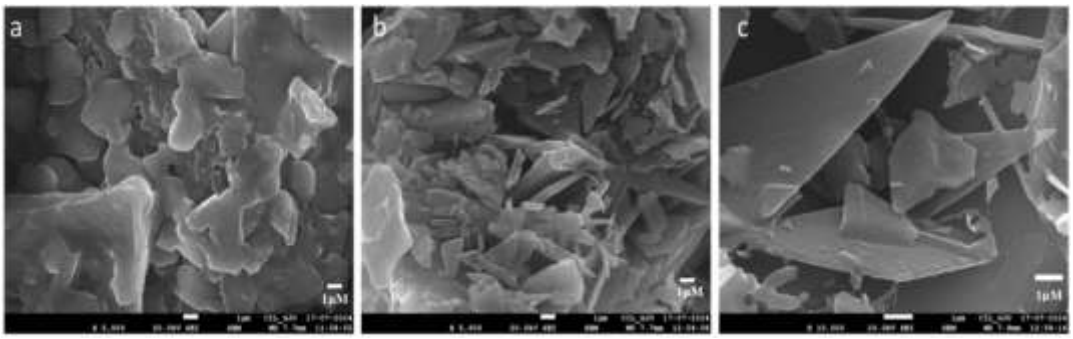

Figure 4: *Fe-SEM images of formed AI-IONPs at a) pH 3 b). pH 6 and c). pH 11.*

Dynamic Light Scattering (DLS):

DLS measurements show average particle sizes of 355 nm at pH 3, 198 nm at pH 6, and 275 nm at pH 11 (Figure 5a, 5b, 5c). The sizes obtained through DLS are larger than those observed in FE-SEM due to nanoparticle agglomeration in solution. At pH 3 and 11 extensive aggregation results in the largest particle sizes, consistent with the irregular morphology seen in FE-SEM. At pH 6, the smallest particle size (198 nm) reflects the uniformity of nanorods, aligning with the FE-SEM observations. These results further emphasize that neutral pH conditions produce the most consistent particle distribution.

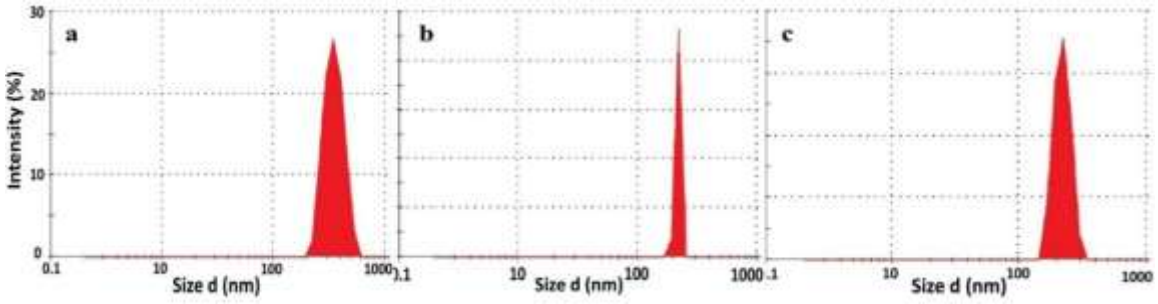

Figure 5: *DLS spectra of AI-IONPs at (a) pH 3 (355 nm), (b) pH 6 (198 nm), and (c) pH 11 (255 nm).*

Zeta-Potential:

The zeta potential measurements indicate the surface charge and colloidal stability of the synthesized nanoparticles. The values are -21.7 mV at pH 3, -28.3 mV at pH 6, and -27.4 mV at pH 11 (Figure 6a,6b,6c). A higher absolute value indicates better stability due to increased electrostatic repulsion. At pH 6, the highest zeta potential corresponds to the most stable nanoparticles, as confirmed by their uniform morphology and minimal aggregation. At pH 3 and pH 11, slightly lower stability is observed, which is consistent with the larger and more irregular particle sizes.

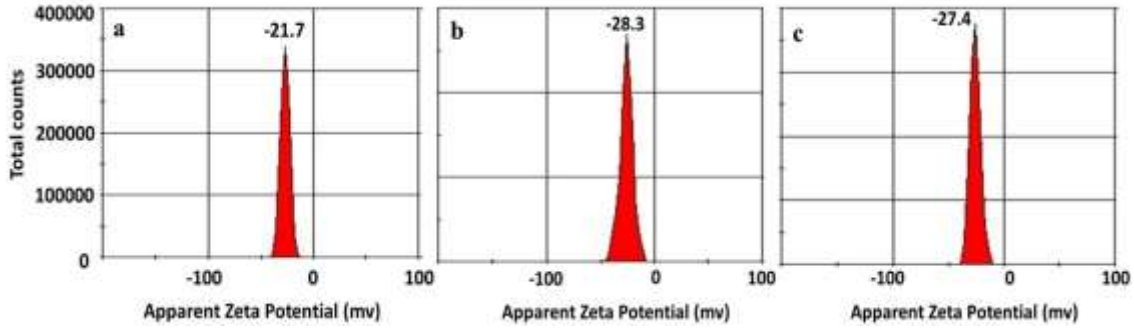

Figure 6: *zeta potential spectra of AI-IONPs at (a) pH 3, (b) pH 6, and (c) pH 11.*

X-ray Diffraction (XRD):

The XRD patterns of the synthesized IONPs at pH 3, 6, and 11 provide insights into their crystalline phases and sizes (Figure 7). The XRD patterns also exhibit well-defined peaks corresponding to planes (012), (104), (110), (113), (024), and (211), which confirm the stable rhombohedral structure of α-Fe_2O_3 (hematite). This identification is supported by the standard JCPDS card no 00-033-0664. The observed diffraction peaks confirm the crystalline nature of the nanoparticles.

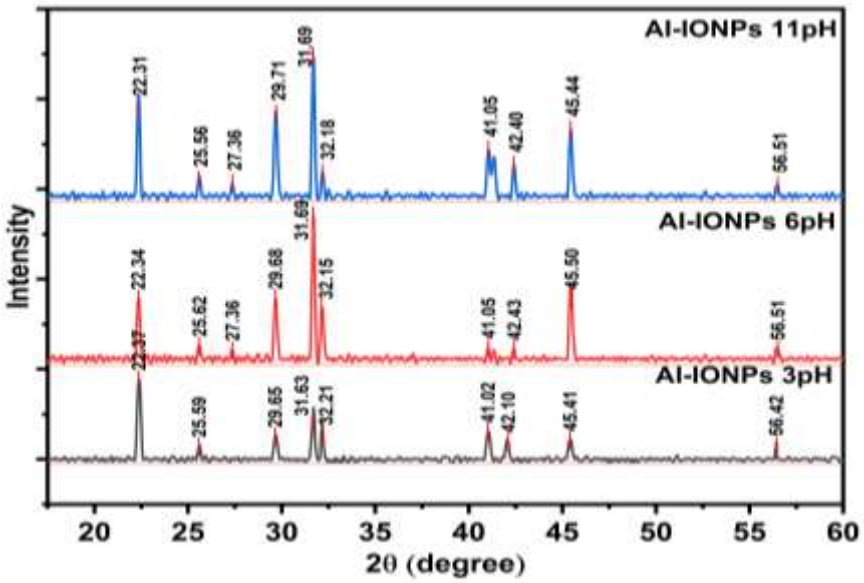

Figure 7: *XRD spectra of formed AI-IONPs at a) pH 3, b). pH 6 and c). pH 11.*

The average size of the highly crystalline Fe_2O_3 nanoparticles was determined using the full width at half maximum (FWHM) and calculated via the Debye–Scherrer equation, providing a precise estimation of nanoparticle dimensions:

$$\boldsymbol{D = \frac{0.89\lambda}{B\cos\theta}}$$

Here, θ represents the Bragg diffraction angle, B denotes the line broadening at half maximum intensity (FWHM) in radians, λ is the X-ray wavelength, and 0.89 corresponds to the shape factor [59]. Using this formula, the calculated average crystalline size for α-Fe2O3 nanoparticles was approximately 30–40 nm. This size range indicates that the nanoparticles are well-ordered and fall within the nanoscale regime, confirming their suitability for various applications.

The lattice constants of the synthesized α-Fe2O3 nanoparticles were found to be a = b = 5.034 Å and c = 13.746 Å, consistent with the rhombohedral hematite structure. The shift in peak positions and uniformity of these lattice parameters across different pH values suggest minimal variation in the fundamental crystalline framework, even as other properties, Characteristics such as particle size and morphology, are governed by the synthesis parameters.

Table 3: *Size calculation from XRD data of IONPs at pH values of 3, 6 and 11.*

	2Ɵ			FWHM			size d (nm)		
Sr. no	**3pH**	**6pH**	**11pH**	**3pH**	**6pH**	**11pH**	**3pH**	**6pH**	**11pH**
1	22.37	22.31	22.33	0.125	0.118	0.093	64.78484	68.62091	87.07039
2	25.59	25.56	25.57	0.14	0.101	0.07	58.18985	80.65441	116.3751
3	29.65	29.71	29.69	0.15	0.15	0.153	54.78564	54.79324	53.71638
4	31.63	31.69	31.69	0.101	0.101	0.072	81.75087	81.76301	114.6953
5	41.02	41.05	41.05	0.25	0.25	0.46	33.9278	33.93113	18.44083
6	45.41	45.5	45.44	0.097	0.13	0.094	88.77994	66.26529	91.62338
7	56.42	56.51	56.51	0.12	0.17	0.08	75.12578	53.05233	112.7362
	Average size						65.33496	62.72576	84.95109

Fourier Transform Infrared (FTIR) spectroscopy:

The synthesized iron oxide nanoparticles (IONPs) were characterized using FTIR spectroscopy in the scanning range of 500–4200 cm^{-1} to identify surface functional groups involved in metal interactions. Furthermore, the presence of surface functional groups in metal interactions can be attributed to the high content of polyphenols, flavonoids, phenols, gallic acid, and nimbins found in *AI* extract. Figure 8 illustrates the FTIR spectra of the AI leaf extract and AI-mediated IONPs synthesized at various pH levels. The graphs demonstrated that the band of various intensities across various wavenumbers. A significant peak was found in the 3325–3700 cm^{-1} range, which corresponds to the polyphenolic group's O–H stretching vibrations. The peak at 2927 cm^{-1} is assigned with the C-H stretching vibration of the methyl or methoxy group which disappears in the acidic medium suggesting that certain functional groups are unstable or undergo modification at lower pH levels. Peaks in the region of 1509–1615 cm^{-1} correspond to carboxylate (C–O and C=O) functional groups, highlighting the potential role of carboxylic acids in reducing and stabilizing the nanoparticles. A distinct peak at ~785 cm^{-1} represents the bending vibration of C=C groups, characteristic of aromatic systems in the extract. The Fe-O-Fe stretching vibrations were observed at 699, 679 and 622 cm^{-1} at the pH of 11, 3 and 6, respectively [60-61].

The intensity and position of O–H, C–H, and carboxylate peaks vary with pH, indicating that these groups are actively involved in stabilizing nanoparticles and are sensitive to the synthesis environment. Fe–O–Fe vibrations confirm the formation of iron oxide nanoparticles at all pH values.

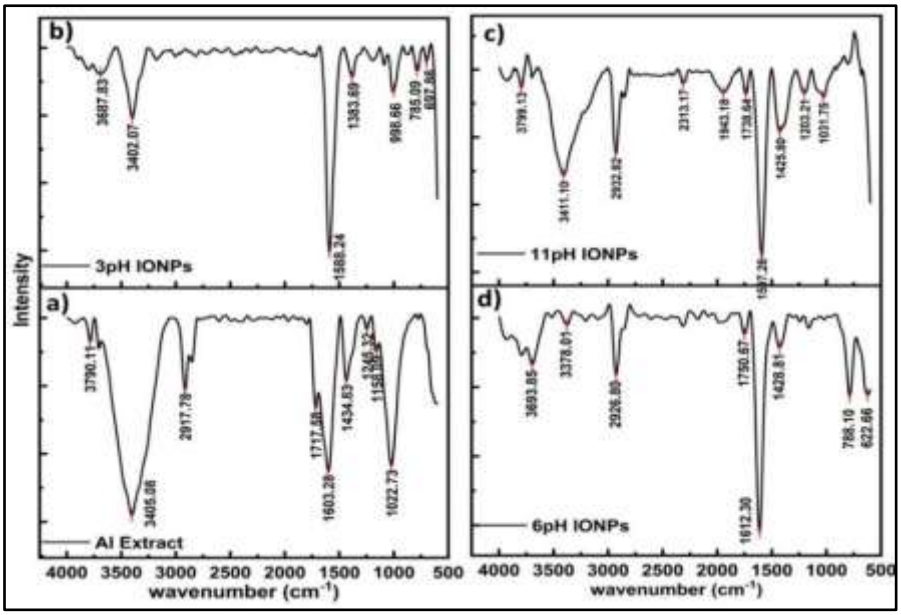

Figure 8: *FT-IR spectra of formed AI-IONPs at a) pH 11 b). pH 3 and c). pH 6.*

Brunauer-Emmett-Teller (BET):

BET analysis was used to examine the surface characteristics of the green-synthesised IONPs, such as surface area, pore size, and volume. Figures 8a, 8b, and 8c show the sample's nitrogen adsorption-desorption isotherm. The adsorption-desorption curves exhibit a type IV isotherm with an H3 hysteresis loop, characteristic of mesoporous materials with slit-shaped pores. Additionally, the data analysis revealed that the mesoporous IONPs had noticeably larger pore widths, pore volumes, and surface areas.

Additionally, the N2 isotherm presented in Figure 9 and Table 4 indicated consistent channels with properly sized pores, alongside a high surface area and pore diameter. The highest surface area (4.31 m^2/g) Pore volume (0.0303 cm^3/g) and pore size at pH 6 (28.129 nm) compared to samples synthesized at pH 3 and 11, suggesting enhanced nanoparticle dispersion and optimized pore formation under neutral conditions.

The lower surface area and smaller pore size suggest limited pore development due to the acidic environment where as a balance in the oxidation and aggregation processes happens at pH6, promoting uniform pore formation. The alkaline environment leads to larger voids but reduced surface area, possibly due to excessive oxidation and particle aggregation, which reduces the overall porosity. The variation in pore size indicates that pH affects the growth mechanism and the arrangement of mesopores during synthesis.

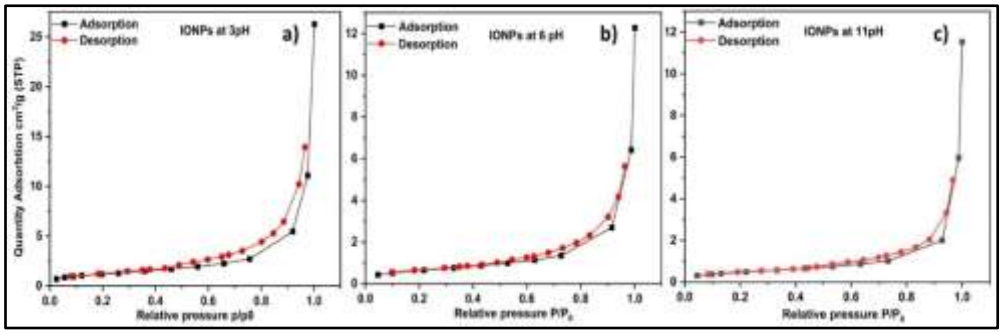

Figure 9: *shows N_2 absorption isotherm curve mesoporous AI-IONPs obtained in a) pH 3 b). pH 6 and c). pH 11 respectively*

Table 4: Experiment results of BET.

Sample	Surface area (m2/g)	Pore size (nm)	Pore Volume (cm3/g)
3 pH	2.32	19.897	0.0116
6pH	4.31	28.129	0.0303
11 pH	1.75	24.016	0.0105

The catalytic activity of *AI*-IONPs for dye degradation:

The catalytic performance of *AI*-IONPs was thoroughly evaluated using two model organic dyes with contrasting ionic properties, Methylene Blue (MB), a cationic dye, and Eosin Yellow (EY), an anionic dye, under varying pH conditions through a Fenton-like oxidation process. This comparison provides insight into the pH-dependent surface interactions and radical generation efficiency of *AI*-IONPs during oxidative degradation. In dilute aqueous media, MB and EY exhibit principal absorption maxima (λ_max) at 664 nm and 520 nm, respectively. MB additionally shows a secondary shoulder near 610 nm, while EY presents one around 485 nm, corresponding to a 0–1 vibronic transition between their ground and excited electronic states. These optical signatures are sensitive to molecular aggregation and electrostatic interactions, which can influence the degradation kinetics. Hence, λ_max values of 664 nm (MB Figure S5) and 520 nm (EY-Figure S6) were selected to monitor their degradation profiles [54,63].

MB degradation:

The degradation efficiency of *AI*-IONPs toward MB was examined at pH 3, 6, and 11 (Figures 10 and 11). In the absence of H_2O_2, the removal efficiencies were 56.87%, 61.86%, and

48.07%, respectively. When H_2O_2 was added, these values increased significantly to 73.93%, 86.60%, and 67.30%. The superior degradation observed at pH 6 can be attributed to the optimal generation of hydroxyl radicals (•OH) and the favourable electrostatic attraction between the positively charged MB molecules and the negatively charged AI-IONP surface. This condition promotes rapid dye adsorption and enhances electron transfer between Fe^{2+}/Fe^{3+} redox couples during the Fenton-like reaction. The kinetic analysis further confirmed that *AI*-IONPs exhibited the highest rate constant at pH 6, highlighting the efficient catalytic conversion of H_2O_2 into reactive radicals.

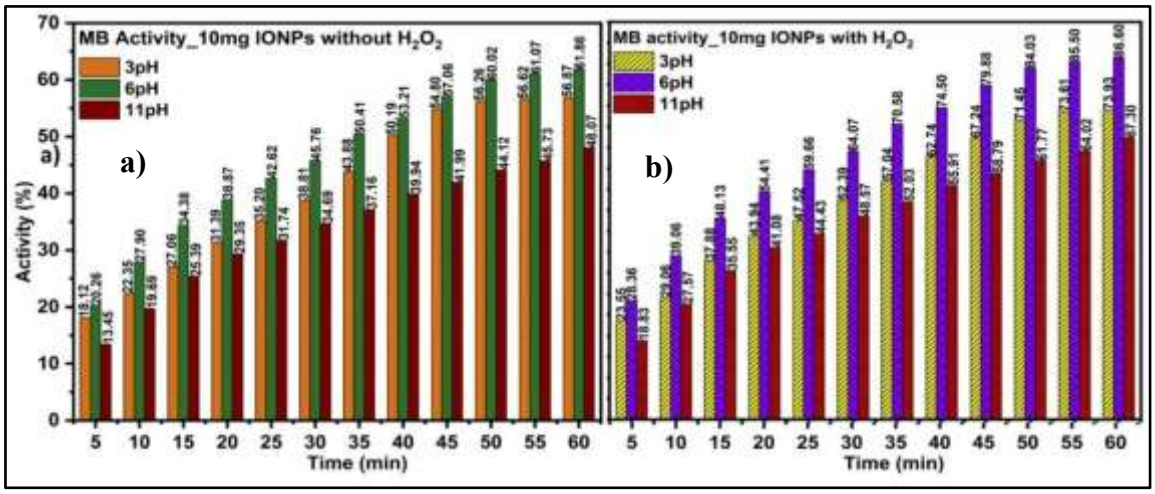

Figure 10: *Histogram of catalytic activity a) without H_2O_2, b) with AI-IONPs against MB dye at pH 3, 6, and 11.*

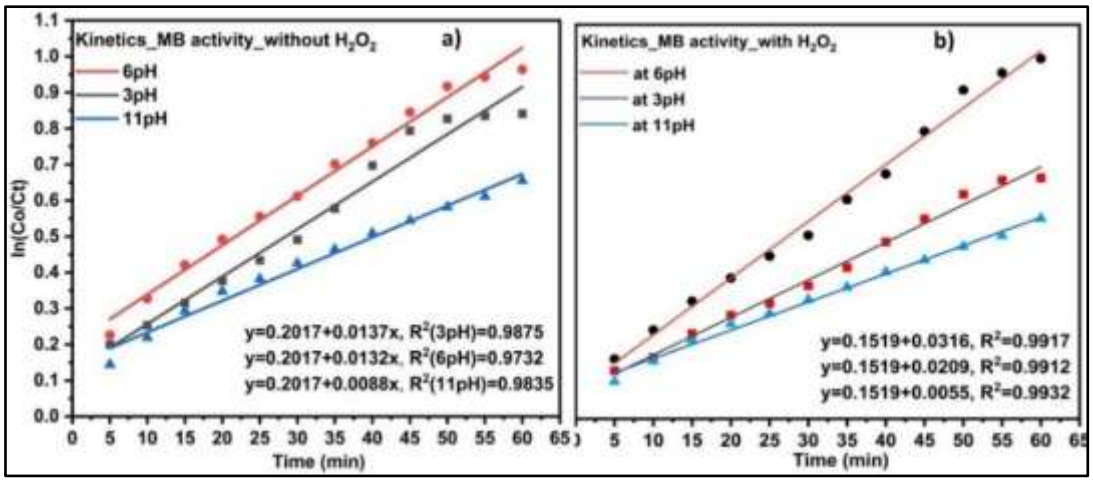

Figure 11: *Kinetics of dye degradation rate with time, b) without H_2O_2 d). With H_2O_2. C) of AI-IONPs against MB dye at pH 3, 6, and 12.*

EY degradation:

A parallel investigation was conducted for EY (Figures 12 and 13). Without H_2O_2, removal efficiencies were 42.97%, 55.32%, and 44.60% at pH 3, 6, and 11, respectively. In the presence of H_2O_2, degradation markedly improved to 75.19%, 82.98%, and 73.59%. Similar to MB, the optimum degradation was achieved at pH 6, demonstrating the universal catalytic capability of AI-IONPs under near-neutral conditions. However, the slightly lower overall degradation of EY compared to MB can be explained by electrostatic repulsion between the negatively

charged EY molecules and the *AI*-IONP surface, which reduces adsorption efficiency. Despite this, the presence of H_2O_2 effectively compensated for this limitation by generating sufficient •OH radicals to oxidize EY into smaller, less toxic intermediates.

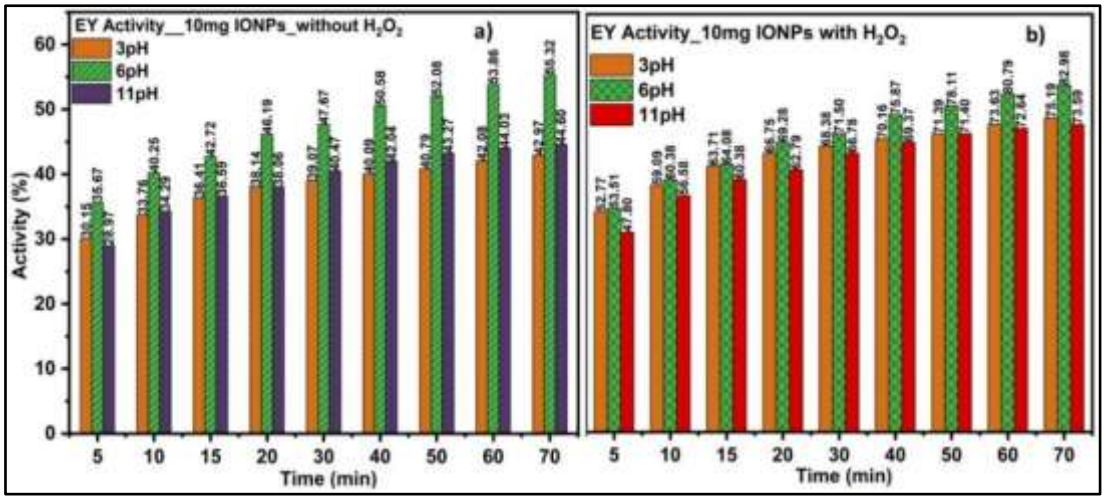

Figure 12: *bar graph of catalytic activity, a) without H_2O_2, c) with H_2O_2 and the kinetics of dye degradation rate with time of AI-IONPs against EY dye at pH 3, 6, and 12.*

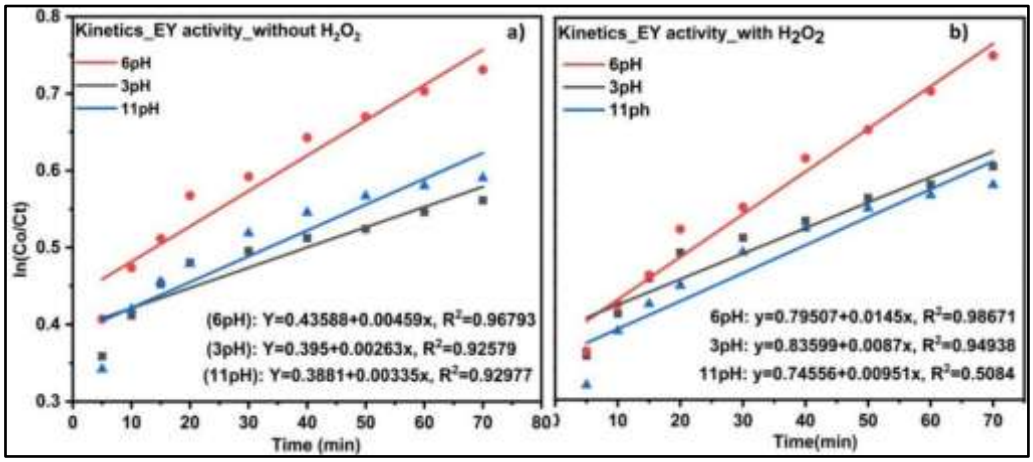

Figure 13: *kinetic of dye degradation rate with time, a) without H_2O_2, b). With H_2O_2. C) of AI-IONPs against EY dye at pH 3, 6, and 12.*

The comparative analysis of MB and EY degradation confirms that *AI*-IONPs exhibit efficient, broad-spectrum catalytic activity toward both cationic and anionic dyes. The higher efficiency for MB indicates the role of electrostatic attraction in enhancing dye adsorption, while the improved EY degradation with H_2O_2 highlights the dominance of •OH radical-driven oxidation. Overall, *AI*-IONPs function as sustainable Fenton-like catalysts with optimal performance at pH 6, demonstrating strong potential for wastewater treatment and environmental remediation.

Antioxidant activity:

As antioxidants, metallic nanoparticles (NPs) can effectively neutralize free radicals such as DPPH, thereby mitigating oxidative damage. In the DPPH assay, the mechanism involves the reduction of the purple-coloured DPPH• radical to its non-radical yellow-coloured DPPH-H form through electron or hydrogen atom donation from antioxidant species such as the

synthesized AI-IONPs [50]. The UV–Vis spectra (Figure 14a) clearly depict this transformation, as evidenced by the gradual decrease in absorbance intensity at 517 nm with increasing nanoparticle concentration.

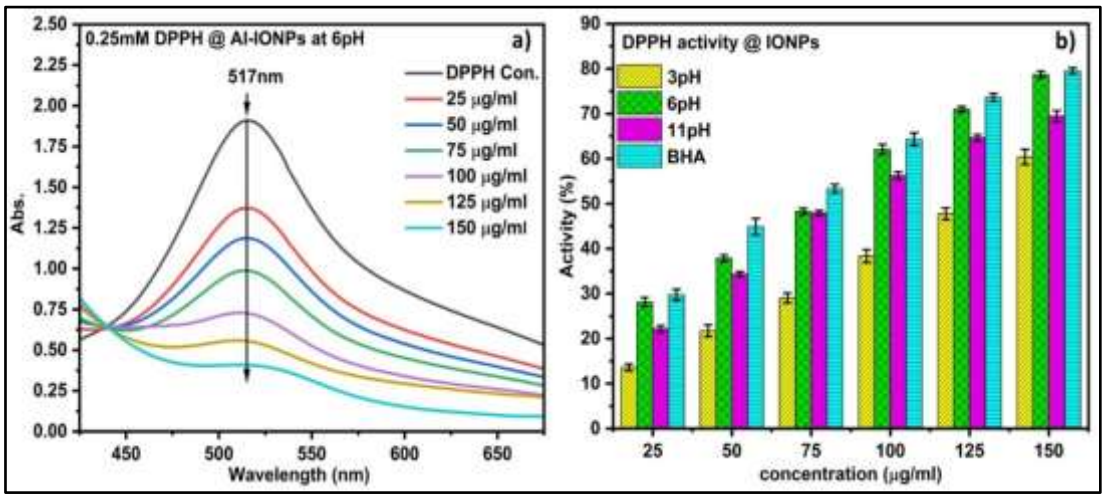

Figure 14: *a). Uv-Vis. Spectra antioxidant activity of AI-IONPs, b). The Histogram of antioxidant activity of AI-IONPs against DPPH at pH of 3, 6 and 11 compared with BHA.*

The corresponding plot (Figure 14b) demonstrates a concentration-dependent increase in radical scavenging efficiency, confirming the strong antioxidant potential of *AI*-IONPs. Furthermore, as presented in Table 5, the antioxidant activity varied with synthesis pH, where IONPs prepared at pH 6 exhibited the highest DPPH scavenging activity compared to those synthesized at pH 3 and 11, indicating that the optimal pH enhances surface reactivity and electron-donating capacity.

Table 5: Antioxidant activity of *AI*-IONPs against DPPH assay with SD

	Antioxidant activity with SD in (%)							
	3pH		**6 pH**		**11 pH**		**BHA**	
Time (min)	**(%)**	**SD**	**(%)**	**SD**	**(%)**	**SD**	**(%)**	**SD**
25	13.6148	0.78	28.1372	1.02	22.1620	0.77	29.7573	1.18
50	21.7456	1.31	37.8484	0.76	34.3476	0.56	44.8936	1.82
75	29.0445	1.09	48.2715	0.73	47.9053	0.56	53.3454	0.94
100	38.3493	1.44	62.0646	1.11	56.2180	0.84	64.3388	1.41
125	47.7727	1.29	70.9740	0.64	64.6576	0.72	73.6065	0.87
150	60.3852	1.69	78.6983	0.73	69.4401	1.24	79.5129	0.69

AI-IONPs synthesized at pH 6 showed the highest antioxidant activity with an IC_{50} of 78.06 µg/mL, lower than those at pH 3 (129.63 µg/mL) and pH 11 (88.64 µg/mL). This value is comparable to the standard antioxidant BHA (69.68 µg/mL) (Figure 15), confirming the strong DPPH radical scavenging ability of IONPs prepared at the optimized pH.

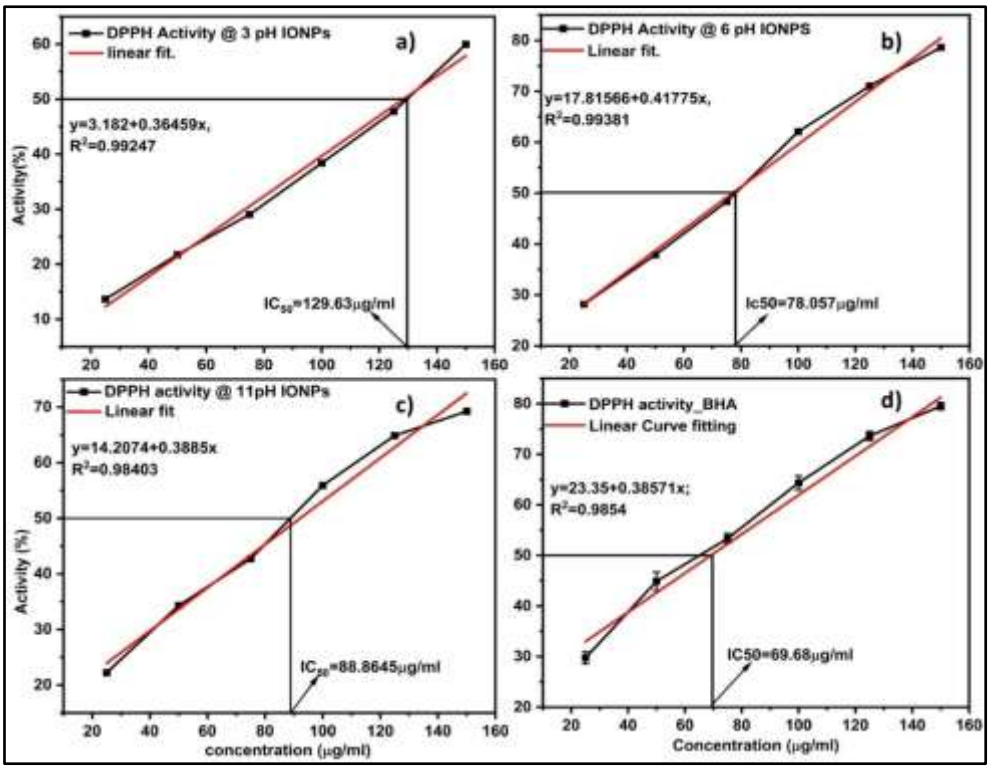

Figure 15: a). The IC50 Value of antioxidant activity of AI-IONPs against DPPH at a). pH 3, b). pH 6 and c). pH 11.

A similar trend was observed in the ABTS assay, which evaluates the ability of antioxidants to quench the blue-green ABTS•$^{+}$ radical cation. The reduction of ABTS•$^{+}$ by AI-IONPs resulted in a noticeable decline in absorbance at 745 nm, as shown in Figure 16a, indicating efficient radical scavenging. The graphical representation in Figure 16b confirms that the antioxidant efficiency of *AI*-IONPs increases proportionally with their concentration.

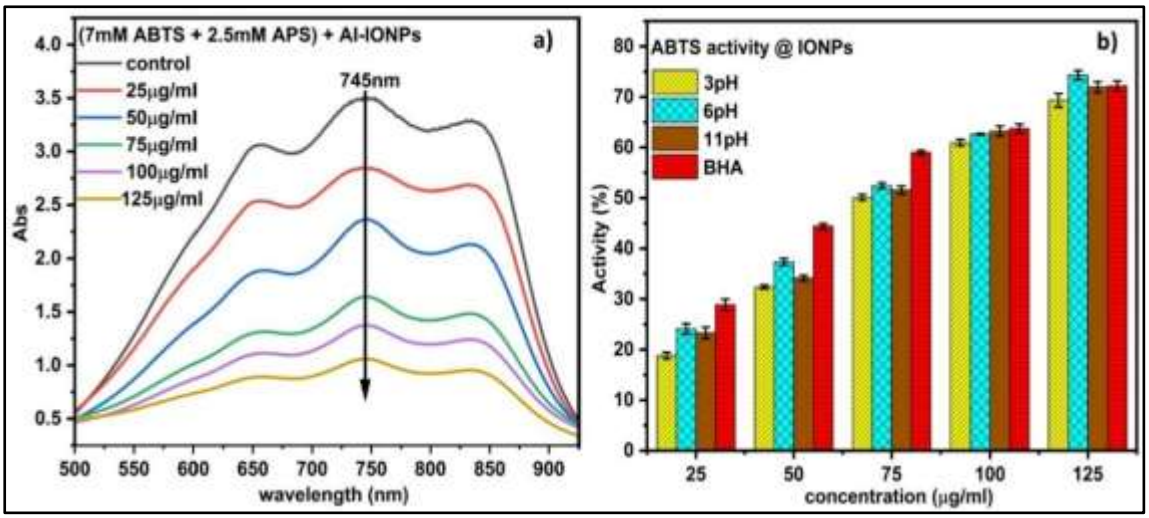

Figure 16: *a). Uv-Vis. Spectra antioxidant activity of AI-IONPs, b). Curve graph of antioxidant activity at pH 3, 6 and 11 compared with BHA against ABTS.*

As summarized in Table 6, the nanoparticles synthesized at pH 6 exhibited superior ABTS scavenging activity relative to those prepared at pH 3 and 11. This enhanced activity at pH 6

can be attributed to the improved crystallinity, smaller particle size, and greater surface availability of active sites, facilitating effective electron transfer to the ABTS•$^{+}$ radicals.

Table 6: Antioxidant activity of *AI*-IONPs against ABTS assay with SD

	Antioxidant activity with SD in (%)							
	3pH		6 pH		11 pH		BHA	
Time (min)	(%)	SD	(%)	SD	(%)	SD	(%)	SD
25	18.8029	0.66	24.1185	1.03	23.3250	1.1473	28.8705	1.11
50	32.3877	0.40	37.3489	0.68	34.1535	0.5545	44.4351	0.55
75	50.1035	0.57	52.4272	0.57	51.5746	0.7920	59.0045	0.43
100	60.9416	0.63	62.6249	0.13	63.2433	0.9805	63.7611	0.86
125	69.3325	1.35	74.2949	0.91	71.9511	1.0554	72.1550	0.99

Similarly, IONPs synthesized at pH 6 exhibited superior ABTS radical scavenging activity with an IC_{50} of 76.21 µg/mL, compared to 82.70 µg/mL (pH 3) and 77.33 µg/mL (pH 11), (Figure 17). This performance is close to that of BHA (60.62 µg/mL), demonstrating excellent antioxidant efficiency of the green-synthesized *AI*-IONPs.

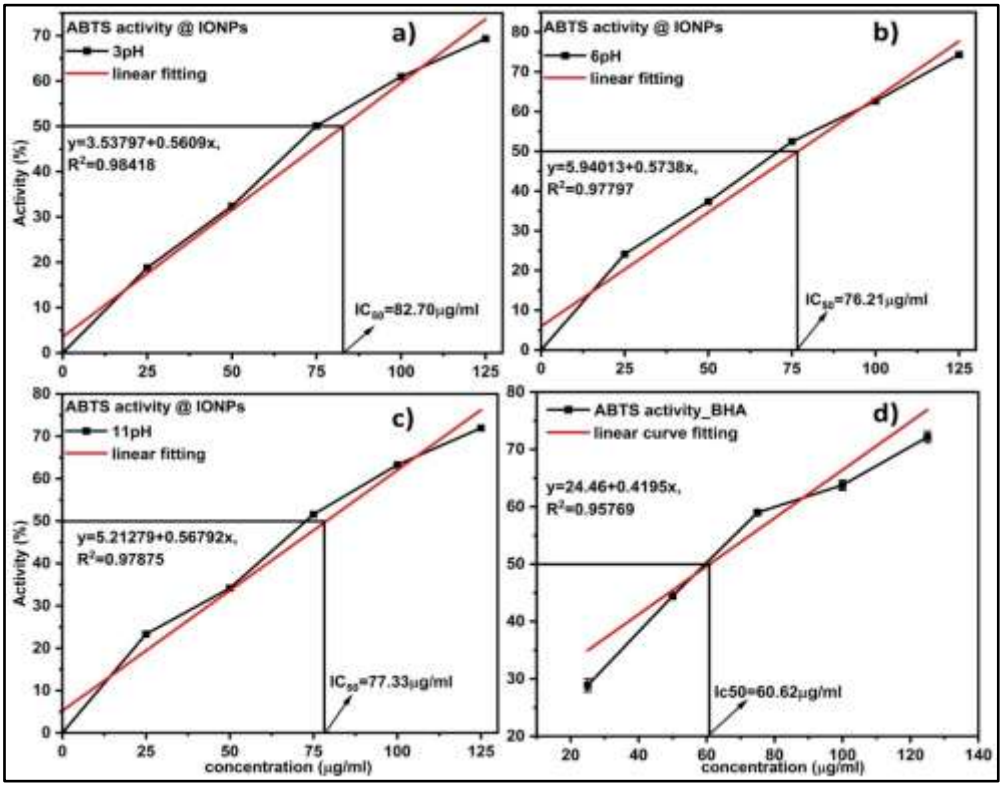

Figure 17: *The graph IC50 Value of antioxidant activity at a). 3 pH b). 6 pH and c). 11 pH and d). Standard BHA.*

Although these activities are nearly similar compared to butylated hydroxyanisole (BHA), which is attributed to bioactive compounds from plant extracts [65]. Utilizing natural antioxidants can mitigate the risk of cancer, heart disease, and chronic disorders. The findings indicate that IONPs are effective in scavenging ROS production and hold promise for

biomedical applications. Therefore, biogenic IONPs could serve as an alternative antioxidant agent [66].

Conclusion:

The IONPs synthesized from *AI* Leaf extract using a green approach are eco-friendly and easy to use without heavy instrumentation and conditions. FT-IR results showed that the active phytochemicals were present in *AI* Leaf extract which effectively works as a reducing and capping agents. Uv-Vis, DLS and Zeta potential results revealed that the IONPs were stable, whereas the XRD showed the orientations of IONPs were rhombohedral with the size of 62.71nm, 65.33nm and 84.95nm at an extract pH of 6, 3 and 11, respectively. Further confirmed by FE-SEM. Synthesized IONPs could efficiently remove the anionic (EY) and cationic (MB) dye with H_2O_2 and without H_2O_2. Additionally, the result shows that H_2O_2 also increase both the kinetics and the degradation of dye up to a certain concentration, because of the scavenging of the hydroxyl radicals by the H_2O_2. The UV-vis graphs for the dye removal efficiency at pH values 6 both with MB and EY dyes, 61.86% and 55.32% without adding H_2O_2. Similarly in the presence of H_2O_2 where the removal efficiency of the dye increases compared to without H_2O_2, with the removal efficiency of 86.60% and 82.98% respectively at room temperature. Prominent antioxidant activities were proven with DPPH and ABTS free radical scavenging activity is 78.66% at 150µg/mL and 69.74% at 125µg/mL. Although these activities are nearly similar compared to butylated hydroxyanisole (BHA), which is attributed to bioactive compounds from plant extracts. Also, the IC50 values for DPPH and ABTS assay are 78.057µg/ml and 70.94µg/ml respectively.

Conflicts of Interest

The authors declare no conflicts of interest.

Acknowledgements

The author thanks the Tarsadia Institute of Chemical Science, and Maliba Pharmacy College Uka Tarsadia University, for materials characterizations. Malti thank to Govt. of Gujarat for financial support under SHODH fellowship (File number KCG/SHODH/2023-24/2023017310). Also thankful to the Institute of Chemical Technology, Mumbai for BET Characterization.

References:

1. Yousaf Khan, Haleema Sadia, Syed Zeeshan Ali Shah et al., *Catalysts*, 2022, 12, 1386. doi.org/10.3390/catal12111386.
2. B. I. Kharisov, H. V. Rasika Dias, O. V. Kharissova, et al.; *RSC Adv*., 2012, 2, 9325–9358. DOI:10.1039/C7RA05302A.
3. D. L. Tejedor, R. Benavent and J. M. Palomo; *Catal. Sci. Technol*., 2018, 8, 1754–1776. doi.org/10.1039/C7CY02259J
4. Laurent S, Forge D, Port M, Roch A, et al.; *Chem Rev*., 2008, 108:2064-2110. DOI: 10.1021/cr068445e.
5. A.V. Nikam, B. L. V. Prasad, and A. A. Kulkarni.; *Cryst. Eng. Comm*, 2018, 20, 5091–5107. https://doi.org/10.1039/C8CE00487K.

6. M. Devi, S. Devi, V. Sharma, N. Rana, et al.; *J. Tradit. Complementary Med*., 2020, 10, 158–165. doi.org/10.1016/j.jtcme.2019.04.007.
7. B. Yuliarto, N. L. W. Septiani, Y. V. Kaneti, et al.; *New J. Chem*., 2019, 43, 15846–15856. doi.org/10.1039/C9NJ03311D
8. Anna Timoszyk; *Bull. Mater. Sci*., 2018 41:154, doi.org/10.1007/s12034-018-1673-4.
9. R. K. Sharma, S. Yadav, R. Gupta and G. Arora; *J. Chem. Educ.*, 2019, 96, 3038–3044. doi.org/10.1021/acs.jchemed.9b00384
10. Khanal LN, Dhakal PP, Kandel MR, et al.; *Inorganics*, 2023; 11(6), 263. doi.org/10.3390/inorganics11060263
11. S. Venkat Kumar, S. Rajeshkumar; *Academic Press*, 2018, Chapter 2, 33-57. doi.org/10.1016/B978-0-12-811487-2.00002-5
12. Harsh Kumar, Kanchan Bhardwaj, Kamil Kuˇca, et al; *Nanomaterials* 2020, 10, 766; doi:10.3390/nano10040766
13. Noruzi, M.; *Bioprocess and Biosystems Engineering*, 2014, 38 (1), 1–14. DOI:10.1007/s00449-014-1251-0
14. Shakeel Ahmed, Annu, Saiqa Ikram, Salprima Yudha S.; *Journal of Photochemistry and Photobiology B: Biology,* 2016, 161, 141-153. doi.org/10.1016/j.jphotobiol.2016.04.034.
15. Mittal, A. K., Chisti, Y., & Banerjee; *Biotechnol adv*. 2013, 31(2), 346-356. DOI:10.1016/j.biotechadv.2013.01.003
16. Maxwell Thatyana, Nondumiso P. Dube, Douglas Kemboi et al., *Nanomaterials*, 2023, 13, 2616. doi.org/10.3390/nano13192616.
17. Kulkarni, N., & Muddapur, U.; *Journal of Nanotechnology*, 2014, 1-8. doi.org/10.1155/2014/510246.
18. L. Huang, X. Weng, Z. Chen, M. Megharaj and R. Naidu. *Spectrochim. Acta, Part A*, 2014, 130, 295–301. DOI: 10.1016/j.saa.2014.04.037
19. S. Saif, A. Tahir and Y. Chen.; *Nanomaterials,* 2016, 6, 1–26. DOI: 10.3390/nano6110209
20. Villagrán Z, Anaya-Esparza LM, Velázquez-Carriles CA, et al.; *Resources,* 2024; 13 (6), 70. doi.org/10.3390/resources13060070
21. Jayanta Kumar Patra and Kwang-Hyun Baek.; *Journal of Nanomaterials*, 2014, 417305, 12. dx.doi.org/10.1155/2014/417305
22. Saeed Ahmadi, Cobra Izanloo.; *Results in Chemistry*, 2023, 6, 101192. doi.org/10.1016/j.rechem.2023.101192
23. S. Machado, W. Stawi´nski, P. Slonina et al.; *Science of the Total Environment*, 2013, 461-462, 323–329. doi:10.1021/acssuschemeng.5b01185
24. Yosmery Vitta, Maice Figueroa, María Calderon, Carlos Ciangherotti.; *Materials Science for Energy Technologies*, 2020, 3, 97-103. doi.org/10.1016/j.mset.2019.10.014.
25. Shuaixuan Ying, Zhenru Guan, Polycarp C. et al.; *Environmental Technology & Innovation*, 2022, 26, 102336. doi.org/10.1016/j.eti.2022.102336.
26. Radulescu D.-M., Surdu V.-A., Ficai, A., et al.; *Int. J. Mol. Sci*. 2023, 24, 15397.doi.org/10.3390/ ijms242015397
27. Enshirah Da'na, Amel Taha and Eman Afkar.; *Appl. Sci*. 2018, 8, 1922. doi.org/10.3390/app8101922.
28. Sada Venkateswarlu, Y. Subba Rao, T. Balaji, B. Prathima, N.V.V. Jyothi.; *Materials Letters*, 2013, 100:241–244. doi.org/10.1016/j.matlet.2013.03.018.

29. V.A. Niraimathee, V. Subha, R.S. Ernest Ravindran and S. Ranganathan., *Int. J. Environment and Sustainable Development*, 2016, 15 (3). doi:10.1504/ijesd.2016.077370
30. Hitesh Rajput**,** Abhitosh Kedia, Dimple Shah, *ECS Journal of Solid-State Science and Technology*," 2023, 11. **doi**:10.1149/2162-8777/ad05b6
31. Henam Sylvia Devi, Muzaffar Ahmad Boda, Mohammad Ashraf Shah, et al.; *Green Process Synth,* 2019; 8:38–45. doi.org/10.1515/gps-2017-0145
32. Prasad C., Gangadhara S. & Venkateswarlu P., *Appl Nanosci*., 2016, 6, 797–802. doi.org/10.1007/s13204-015-0485-8
33. Muhammad Aqib Shabbir, Muhammad Naveed, Shafiq ur Rehman, Noor ul Ain, et al.; *ACS Omega,* 2023, 8, 33358-33366. doi.org/10.1021/acsomega.3c02744
34. Bharti & Ishani Khurana & Ajay Kumar Shaw; *water Air Soil Pollut*., 2018 229: 17. doi.org/10.1007/s11270-017-3664-2
35. Hsing-Lung Lien, Yu-Sheng Jhuo, and Li-Hua Chen.; *Environmental Engineering Science*, 2007, 24, 1. doi:10.1089/ees.2007, 24, 21.
36. E. Demangeat, M. Pedrot, A. Dia, et al.; *Nanoscale Adv*., 2021, 3, 2017–2029. doi:10.1039/d0na00825g
37. Shuli Yao, Shaohu Ouyang, Qixing Zhou, et al.; *Environmental Research*, 2024, 263, 1, 120009. doi.org/10.1016/j.envres.2024.120009.
38. Shannon, M., Bohn, P., Elimelech, M. et al*.; Nature*, 2008*,* 452, 301–310. doi.org/10.1038/nature06599
39. Zhang Wx., *Journal of Nanoparticle Research*, 2003, 5, 323–332. doi.org/10.1023/A:1025520116015
40. Sharma S., Bhattacharya A.; *Appl Water Sci.*, 2017, **7**, 1043–1067. doi.org/10.1007/s13201-016-0455-7.
41. Hao Zhou, Shikang Wu, Yaoyu Zhou, et al.; *Environment International*, 2019, 128, 77-88. doi.org/10.1016/j.envint.2019.04.006.
42. E. Routoula and S. V. Patwardhan; *Environ. Sci. Technol*.," 2020, 54, 647–664. doi.org/10.1021/acs.est.9b03737.
43. Olivia A. Attallah, Medhat A. Al-Ghobashy, Marianne Nebsen, and Maissa Y. Salem; *RSC Adv*., 2016, 6, 11461. DOI:10.1039/c5ra23452b.
44. Abderrazzak Adachi, Faiçal El Ouadrhiri, Ebraheem Abdu Musad Saleh, et al.; *SN Applied Sciences* 2023, 5:342. doi.org/10.1007/s42452-023-05543-0
45. Anup Adhikari, Kisan Chhetri, Debendra Acharya; *Catalysts* 2022, 12, 1188. doi.org/10.3390/catal12101188
46. Saleem S, Muhammad G, Hussain MA, Bukhari; *Phytotherapy Research*, 2018; 32: 1241-1272. doi.org/10.1002/ptr.6076
47. Wanakai, S.I., Kareru, P.G., Makhanu, D.S. et al.; *SN Appl. Sci.* 2019, 1, 1148. doi.org/10.1007/s42452-019-1203-z
48. Mohamed Hosny, Abdelazeem S. Eltaweil, Mohamed Mostafa, et al.; *ACS Omega*, 2022, 7, 3121-3133. doi.org/10.1021/acsomega.1c06714
49. Fazli Khuda, Meshal Gul, Atif Ali Khan Khalil, et al.; *ACS Omega*, 2023, 8**,** 30221-30230. doi.org/10.1021/acsomega.3c02928
50. Elena N. Hristea, Miron T. Caproiu, Gabriela Pencu; *Int. J. Mol. Sci*, 2006, 7, 130-143. doi.org/10.3390/i7050130

51. Nikolaos Nenadis, Lan-Fen Wang, Maria Tsimidou, And Hong-Yu Zhang; *J. Agric. Food Chem.*, 2004, 52, 4669-4674. doi.org/10.1021/jf0400056
52. N.Nagar, V.Devra, *Materials Chemistry and Physics (Elsevier)*, 2018, 213, 44-51. doi.org/10.1016/j.matchemphys.2018.04.007
53. M.Harshiny, C.N. Iswarya, M. Matheswaran, *Powder Technology*, 2015, 286,744-749. doi.org/10.1016/j.powtec.2015.09.021
54. P. Balu, I. V. Asharani, D. Thirumalai; Journal of Materials Science: *Materials in Electronics*, 2020, 31, 10669–10676. doi.org/10.1007/s10854-020-03616-z
55. Louisah M. Mahlaule-Glory, Sabetha Mapetla, Aubrey Makofane, et al.; *Heliyon*, 2022, 8, 10536. doi.org/10.1016/j.heliyon.2022.e10536
56. Swaha Satpathy, Arjun Patra, Bharti Ahirwar & Muhammad Delwar Hussain; *Artificial Cells; Nanomedicine, And Biotechnology*, 2018, (5), 1-16. doi.org/10.1080/21691401.2018.1489265.
57. Zhang P, Tan X, Liu S, Liu Y, Zeng G, Ye S; *Chem Eng J*. 2019, 378:122141. doi.org/10.1016/j.cej.2019.122141
58. Li H, Shi B, Fu X, Zhang H, Yang H; *J Environ Chem Eng*. 2023, 11(3):109998. doi.org/10.1016/j.jece.2023.109998
59. Mehar Rizvi, Nikita Tiwari, Anil Mishra, and Renu Gupta; *ACS Omega*, 2022, 7, 31667-31681. doi.org/10.1021/acsomega.2c00966
60. Henam Sylvia Devi, Muzaffar Ahmad Boda, Mohammad Ashraf Shah, et al.; *Green Process Synth,* 2019; 8: 38–45. doi.org/10.1515/gps-2017-0145
61. Ch. Prasad, S. Gangadhara, P. Venkateswarlu; Appl Nanosci 2016, 6:797–802. doi10.1007/s13204-015-0485-8
62. M.M. Alam, Mohammed M. Rahman, M.T. Uddin, et al.; *Current Research in Biotechnology*., 2020 2, 176–186. doi.org/10.1016/j.crbiot.2020.11.003
63. Waleed Khalid Hamood Al-Behadili, Yaqoob M. Jawad, Waleed S. Abdul Whaab; *J. Med. Chem. Sci.* 2023, 6 (2) 322-334. doi.org/10.26655/JMCHEMSCI.2023.2.13
64. Anju Srivastava, Sriparna Dutta and Reena Jain; *RSC Sustainability*, 2023, 1, 2261–2269. doi: 10.1039/d3su00246b.
65. Mervat F. Zayed, Ranaa A. Mahfoze, Salah M. El-kousy, Emad A. Al-Ashkar; *Colloids and Surfaces A: Physicochemical and Engineering Aspects*, 2020, 585, 124167, doi.org/10.1016/j.colsurfa.2019.124167
66. Luca Valgimigli, Andrea Baschieri and Riccardo Amorati; *J. Mater. Chem. B*, 2018, 6, 2036. DOI:10.1039/c8tb00107c